




# NiS nanoparticles assembled on biological cell walls-derived porous hollow carbon spheres as a novel battery-type electrode for hybrid supercapacitor

Dan Wu<sup>1</sup>, Hongyang Yu<sup>1</sup>, Chuanxin Hou<sup>1</sup>, Wei Du<sup>1,\*</sup> , Xinhui Song<sup>1</sup>, Tiansha Shi<sup>1</sup>, Xueqin Sun<sup>1</sup>, and Bing Wang<sup>2</sup>

<sup>1</sup>School of Environment and Material Engineering, Yantai University, Yantai 264005, China

<sup>2</sup>CAS Key Laboratory for Biomedical Effects of Nanomaterials and Nanosafety, Institute of High Energy Physics, Chinese Academy of Sciences, Beijing 100049, China

Received: 10 April 2020

Accepted: 28 June 2020

Published online:  
7 July 2020

© Springer Science+Business  
Media, LLC, part of Springer  
Nature 2020

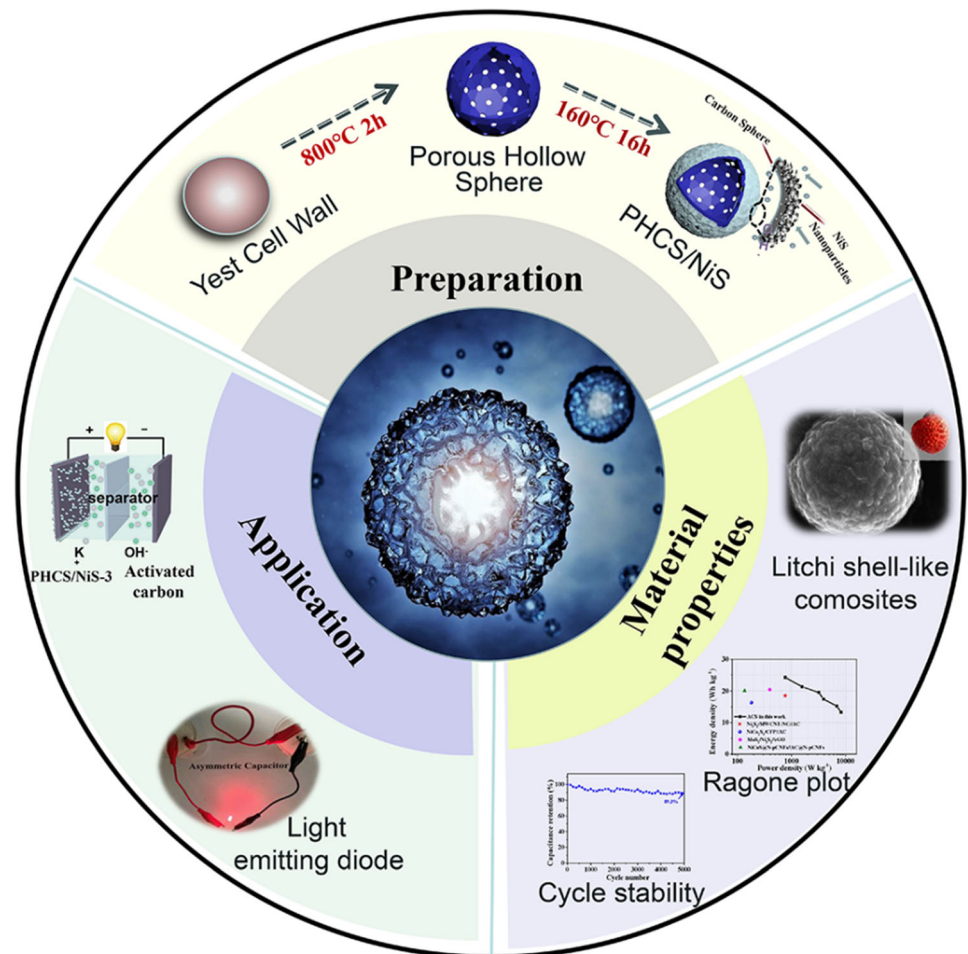
## ABSTRACT

Designing a battery-type electrode material with high electrochemical performance based on eco-friendly and sustainable strategy has great significance for the development of supercapacitors. Herein, NiS nanoparticles are deposited on the surface of the porous hollow carbon spheres (PHCSs) derived from inexpensive and pollution-free yeast cells wall by an in situ hydrothermal process, forming a litchi shell-like three-dimensional (3D) double-shell structure. The PHCSs as a carbon substrate can effectively suppress the aggregation of NiS nanoparticles and ensure more ground storage sites to enhance the performance of the electrode material. More notably, the reaction concentration of nickel ion has a remarkable effect on the electrochemical performance of composites. The optimized sample shows a high specific capacity of  $531.5 \text{ C g}^{-1}$  at  $1 \text{ A g}^{-1}$ , excellent rate capability of  $412.1 \text{ C g}^{-1}$  at  $10 \text{ A g}^{-1}$  and outstanding cycling life span of 83.3% after 5000 cycles. Furthermore, the assembled hybrid device delivers a high energy density of  $24.4 \text{ Wh kg}^{-1}$  at a power density of  $767 \text{ W kg}^{-1}$  and an excellent cycle stability by delivering 89.3% capacitance retention after 5000 ultralong cycles. This work offers a feasible strategy to synthesize economical and efficient electrode materials and demonstrates its enormous potential in energy storage.

Address correspondence to E-mail: duwei@ytu.edu.cn

## GRAPHIC ABSTRACT

A novel NiS/porous hollow carbon sphere composite with double-shell structure was synthesized by a green and available self-template method, which exhibits superior supercapacitor performance.



## Introduction

Driven by the rapid growth of renewable and sustainable energy demand and the burden of continued environment degradation, researchers have developed energetically a new generation of environmentally friendly and high-performance energy storage systems [1–10]. Supercapacitors (SCs) have generated considerable interest owing to advanced characteristics, such as high power density, rapid charging, pollution-free operation and ultralong cycle life span (> 100,000 cycles) [11–13]. They properly make up for

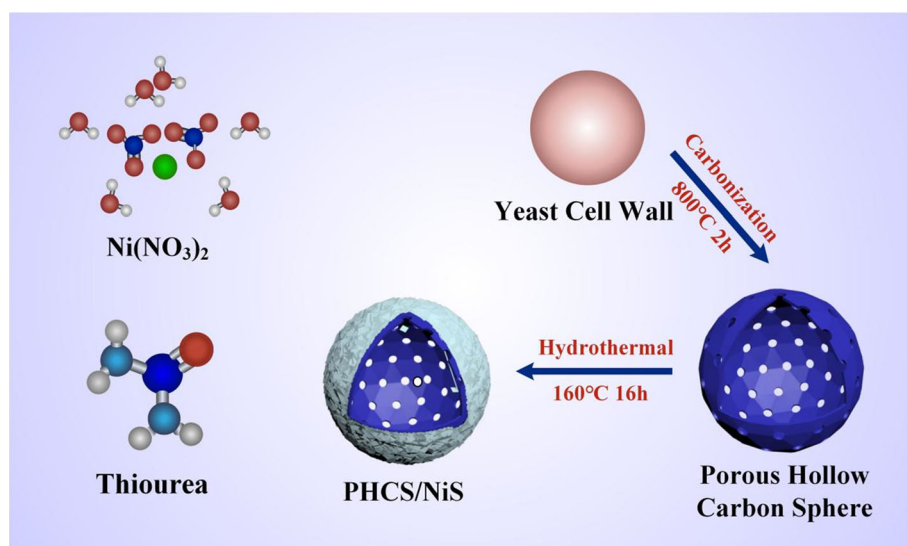
the inadequacy of traditional capacitors and batteries [14]. Nevertheless, supercapacitors still suffer from the inherent disadvantage of low energy density [15]. Thus, much attention was paid to pursue superior supercapacitors with high energy density, without sacrificing their power density and life span in the past decades. Hybrid supercapacitors composed of capacitive and battery-type electrodes present a new opportunity to develop SCs with higher energy density by delivering a large voltage window and high capacity [16, 17].

Recently, tremendous efforts have been focused on designing high-performance electrode materials of hybrid devices. As a new type of battery-type electrode material, transition metal sulfides have been extensively studied by researchers [18, 19]. In particular, NiS has been recognized as a potential anode material because of its excellent redox reversibility, low toxicity and high conductivity [20]. The various oxidation states at the crystal interface of NiS enable nickel ions ( $\text{Ni}^{2+}$ ) to have more abundant and active redox reactions [21]. Compared with the corresponding NiO and  $\text{Ni}(\text{OH})_2$ , it has a lower band gap, which is conducive to electron transition to significantly enhance the conductivity [22, 23]. Meanwhile, the substitution of sulfur for oxygen can provide a more flexible structure because sulfur is less electronegative than oxygen, preventing the collapse of the structure owing to the stretching between the layers [24]. So far, different microstructures of NiS have been prepared, including NiS nanorods [25], NiS nanoparticles [26], NiS nanoflakes [27], flower-like  $\beta$ -NiS [28], hierarchical hollow cube-like NiS [29] and hierarchical nest-like  $\text{Ni}_3\text{S}_2$ @NiS [30]. However, NiS is still affected by the huge volume changes during the intercalation/deintercalation, which leads to structural fracture and poor connectivity of electrode materials resulting in a drop in capacity [31]. To alleviate the mentioned problem, numerous researchers have combined structurally stable carbon materials with NiS to enhance chemical stability and electrical conductivity [32, 33]. Cai et al. [34] reported a self-assembly synthesis method that does not require a binder to anchor NiS nanoparticles on the reduced graphene oxide (rGO) aerogels, which exhibits an excellent capacitance value of  $852 \text{ F g}^{-1}$  at  $2 \text{ A g}^{-1}$ . Sun et al. [35] successfully compounded  $\alpha$ -NiS in carbon nanorods by phase-controlled method, and the composite prepared possesses outstanding electrochemical properties. The specific capacitance reached  $957 \text{ F g}^{-1}$  at  $1 \text{ A g}^{-1}$  and barely decreased during the 2000 charging/discharging cycles. B. Joji Reddy and colleagues [36] fabricated a NiS/N-doped graphene composite as positive material with a high specific capacitance of  $1120 \text{ F g}^{-1}$  at  $1 \text{ A g}^{-1}$  and outstanding electrochemical stability of 82% initial capacitance over 3000 cycles. Among numerous carbon materials, porous hollow carbon spheres (PHCSs) stand out owing to the typical spatial structure and high chemical stability than other materials [37].

Inspired by yeast cell walls that are widely used in food production, animal immunity and environmental fields, the macromolecular saccharide polymers extracted from them are selected as carbon framework to fabricate electrode materials owing to the following advantages. On the one hand, yeast cell walls possess an ideal natural hollow structure: inner cavity acting as ion repositories can quickly provide electrolyte ions for electrochemical reactions; carbon shell with good electrical conductivity facilitates electron transfer. Simultaneously, abundant functional groups distributed on the surface can also improve the wettability of active materials [21]. On the other hand, they are readily available from a variety of raw materials, such as starch, liquor and waste water [38]. The low cost, easy to regenerate, green and pollution-free properties are important for the preparation process of the electrode materials. Up to now, the attempts for porous hollow carbon spheres incorporating with nickel sulfide have been scarce.

In this work, a green and available self-templating method is proposed to synthesize a 3D double-shell structure of PHCSs/NiS composite electrode materials. The PHCSs obtained from readily available and pollution-free yeast cell walls provide support for NiS accompanied with dramatic volume change. NiS nanoparticles deposited on the PHCSs by a simple in situ hydrothermal method make considerable capacitive contribution, improving the electrochemical performance of the materials. In addition, the thickness of deposited NiS nanoparticles can be tuned by adjusting the addition of  $\text{Ni}^{2+}$  concentration. The resulting composite shows a remarkable specific capacity of  $531.5 \text{ C g}^{-1}$  at  $1 \text{ A g}^{-1}$  and excellent cycle life (83.3% capacitance retention after 5000 charge/discharge cycles). A maximum energy density of  $24.3 \text{ Wh kg}^{-1}$  for the prepared hybrid device is achieved at a power density of  $767 \text{ W kg}^{-1}$  and maintains  $13.3 \text{ Wh kg}^{-1}$  at  $8263 \text{ W kg}^{-1}$ . This strategy for designing and manufacturing composite electrodes using universal, renewable materials sheds light on the development of next-generation advanced supercapacitors.

**Figure 1** Schematic diagram of the process of PHCSs/NiS composites.



## Experimental

### Materials

The yeast cell walls were purchased from Yantai Huahai Biological Products Co., Ltd., China. All chemicals used in the experimental process were of AR grade, without any purification.

### Preparation of porous hollow carbon sphere/NiS composites

The schematic diagram of preparing PHCSs/NiS composites is shown in Fig. 1. Yeast cell walls were washed several times with deionized water to eliminate impurities and thoroughly dried at 80 °C overnight. The dried yeast cell walls were carbonized at 800 °C for 2 h (5 °C min<sup>-1</sup>) under nitrogen atmosphere. Then, 3 mmol Ni (NO<sub>3</sub>)<sub>2</sub> and 12 mmol thiourea were dispersed into 30 mL of ethylene glycol solution to obtain a transparent green solution. The as-prepared PHCS (100 mg) was slowly added to the above green solution. After 30 min of ultrasound, the mixed solution was transferred to a 100-mL Teflon-lined stainless steel autoclave and kept at 160 °C for 16 h. After naturally cooling to room temperature, the as-obtained composites were filtered, washed three times with deionized water and dried at 80 °C for 12 h, labeled as PHCSs/NiS-3.

In the following experiments, the other two composites were obtained by adding different amounts (2 mmol and 4 mmol) of Ni(NO<sub>3</sub>)<sub>2</sub>, which were labeled as PHCSs/NiS-2 and PHCSs/NiS-4,

respectively. For comparison, pure NiS was also fabricated by the similar manner of preparing the PHCSs/NiS-3, but without the PHCSs substrate.

### Material characterizations

The morphology and microstructure of samples were characterized by scanning electron microscopy (SEM, JSM-7610F, Japan) and transmission electron microscopy (TEM, JEM-2100, Japan). X-ray diffraction (XRD, Shimadzu XRD-7000, Cu K $\alpha$ ,  $\lambda = 0.15418$  Å) was used to detect structures. Measurement of Fourier transform infrared spectroscopy (FTIR) was carried out on Shimadzu IR Prestige-21 using KBr powder tableting method. X-ray photoelectron spectroscopy (XPS) spectra were conducted by Thermo Fisher Scientific ESCALAB 250Xi instrument with monochromatic Al K $\alpha$  radiation source.

### Electrochemical measurements

The electrochemical characterizations were acquired by a CHI660D instrument (Shanghai Chenhua Instruments Co., China). In a three-electrode system, the prepared PHCSs/NiS electrode as a working electrode, the saturated calomel electrode (SCE) and platinum foil as reference electrode and counter electrode. Typically, the working electrode was prepared by mixing 80 wt% active materials, 10 wt% acetylene black and 10 wt% polyvinylidene fluoride to form homogenous mixture. The mixture was then loaded onto the nickel foam with a coating mass of about 3 mg. Cyclic voltammetry (CV) was performed

at a voltage window from 0 to 0.5 V. Galvanostatic charge–discharge (GCD) was performed at current densities of 1–10 A g<sup>-1</sup>. Electrochemical impedance spectroscopy (EIS) was tested at 5 mV amplitude from 100 kHz to 0.01 Hz.

The hybrid device was fabricated using PHCSs/NiS-3 composites and commercial activated carbon (AC) as anode and cathode. Reference PHCSs/NiS-3 anode, the cathode were prepared. The mass distribution of two electrodes was calculated by Eq. (1) [39]:

$$\frac{m_+}{m_-} = \frac{C_{s-} \times \Delta V_-}{C_{s+} \times \Delta V_+} \quad (1)$$

where + and - indicate the positive and negative electrodes,  $C_s/F \text{ g}^{-1}$  is the specific capacitance,  $\Delta V/V$  is the potential window of electrode and  $m/g$  represents the loading mass of active materials.

The specific capacity of the supercapacitors was determined from GCD curves by Eqs. (2) and (3) [40]:

$$C_q = \frac{I \times \Delta t}{m} \quad (2)$$

where  $C_q/C \text{ g}^{-1}$  represents the specific capacity of the electrode,  $I/A$  is the current density,  $\Delta t/s$  is the discharge time and  $m/g$  represents the loading mass of active material.

$$C_m = \frac{I \times \Delta t}{3600 \times m} \quad (3)$$

where  $C_m/m \text{ Ah g}^{-1}$  represents the specific capacity of the electrode,  $I/mA$  is the current density,  $\Delta t/s$  is the discharge time and  $\Delta V/V$  refers the operating voltage.

The specific capacitance ( $C_s/F \text{ g}^{-1}$ ) of the electrode materials was determined from GCD curves by Eq. (4) [40]:

$$C_s = \frac{I \times \Delta t}{m \times \Delta V} \quad (4)$$

where  $I/A$  represents the current density,  $\Delta t/s$  represents the discharge time,  $\Delta V/V$  represents the operating voltage,  $m/g$  is the loading mass of active material.

The energy density ( $E/Wh \text{ kg}^{-1}$ ) and power density ( $P/Wh \text{ kg}^{-1}$ ) of the hybrid devices were determined using Eqs. (5) and (6) [41]:

$$E = \frac{1}{2} C_s \Delta V^2 \quad (5)$$

$$P = \frac{E}{\Delta t} \quad (6)$$

## Results and discussion

### Material characterizations

The morphologies of PHCSs and PHCSs/NiS composites are presented in Fig. 2. As shown in Fig. 2a, the majority of carbonized yeast cell walls still maintain regular spherical structure with a size of 2–3  $\mu\text{m}$ . From the broken parts of the sphere enlarged in Fig. 2b, the PHCSs present a hollow internal structure and rich porous morphology on the surface of the shell. The formation of porous morphology is attributed to the rapid decomposition of polysaccharides (such as  $\beta$ -glucan and mannan) in the yeast cell walls into monosaccharides and oligosaccharides during the pyrolysis process [42]. In the image of the PHCSs/NiS-2 sample (Fig. 2c), NiS particles were sparsely distributed over the shell of PHCS, which is because the low concentration of  $\text{Ni}^{2+}$  results in the generation of fewer NiS particles during hydrothermal process. Differently, NiS particles are uniformly accumulated on the carbon spheres in the PHCSs/NiS-3 sample, forming a rough surface that like litchi shell structure in Fig. 2d, e. This proper deposition thickness of the NiS nanoparticles not only is conducive to maintaining the stability of the structure, but also effectively increases the number of active sites to expand the contact space between the electrode and electrolyte [43]. With the increase in  $\text{Ni}^{2+}$  concentration, excessive NiS particles accumulate on the shell in the PHCSs/NiS-4 sample (Fig. 2f), which is detrimental to the transmission of electrons, resulting in a decrease in conductivity. To investigate the elemental distribution of the composite, the elemental mapping of PHCSs/NiS-3 sample is presented in Fig. 2g–i. The C, Ni and S elements were uniformly accumulated on the carbon sphere shell, demonstrating the NiS particles were successfully introduced into the surface of the PHCSs.

Figure 3 displays the TEM images of PHCSs, pure NiS particles and PHCSs/NiS-3 composite. As can be seen from Fig. 3a, b, PHCSs show a regular spherical morphology and an internal hollow structure, which is consistent with the SEM analysis. The pure NiS presents nanoscale irregular particles in Fig. 3c. After compounding, the shell of the PHCSs is covered with the uniformly distributed NiS particles with an average size of 100 nm, as shown in Fig. 3d, e. The uniquely designed structure can effectively alleviate the drawbacks of volume expansion of pure NiS to

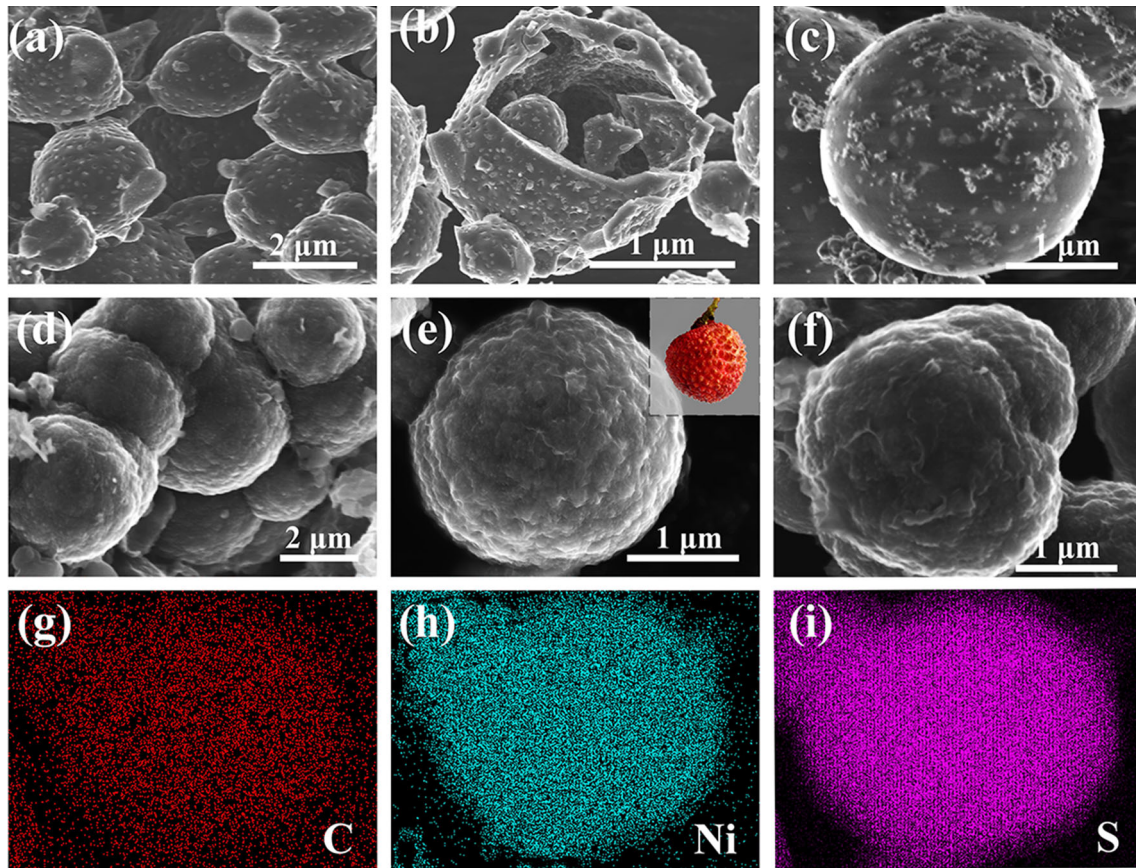


**Figure 2** SEM images of **a, b** PHCSs, **c** PHCSs/NiS-2, **d, e** PHCSs/NiS-3, **f** PHCSs/NiS-4, **g, h, i** elemental mapping of C, Ni and S of **e**.

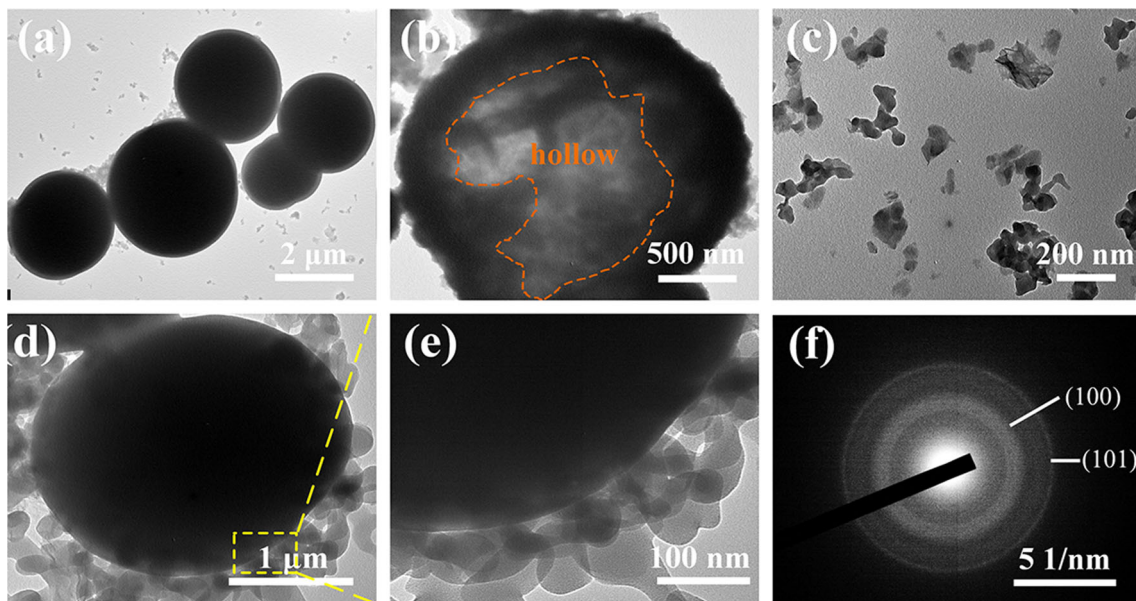
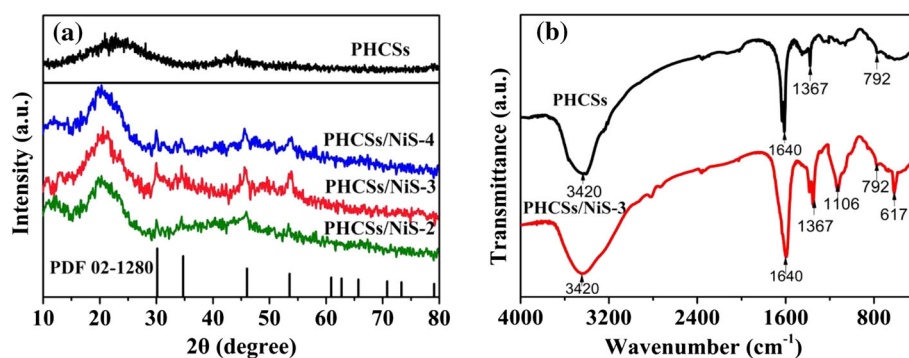


**Figure 3** TEM images of **a, b** PHCSs, **c** pure NiS, **d, e** PHCSs/NiS-3, **f** SADE pattern of PHCSs/NiS-3.

**Figure 4** a XRD patterns of PHCSs, PHCSs/NiS-2, PHCSs/NiS-3 and PHCSs/NiS-4, b FTIR spectra of PHCSs and PHCSs/NiS-3.



improve the electrochemical stability of electrodes. The selected area electron diffraction (SAED) pattern reveals that the PHCSs/NiS-3 composite is an amorphous material (Fig. 3f). The two blurred diffraction rings are confirmed as the (100) and (101) planes of NiS phase, respectively, which agrees well with the results of XRD analysis.

Figure 4a exhibits the structural characterization of materials by XRD patterns. The broad peaks located at 25° and the inconspicuous peak located at 43° of the PHCSs represent the graphitic (002) and (100) planes, denoting the amorphous state of the carbon material [44, 45]. Different amounts of Ni(NO<sub>3</sub>)<sub>2</sub> were used in the synthesis process to obtain three different composite samples. There are four diffraction peaks at 30.2°, 34.7°, 46°, 53.5° in the patterns of all PHCSs/NiS composites, which correspond to the (100), (101), (102) and (110) planes of NiS phase, respectively (JCPDS 02-1280) [23, 46]. The results confirm that the existence of PHCSs substrate did not change the crystal structure of the NiS. Moreover, Fig. 4b exhibits the FTIR spectra of PHCSs and PHCSs/NiS-3. There are same peaks at 3420 and 1367 cm<sup>-1</sup> of the two samples, indicating the –OH bending vibration and stretching vibration. The absorption peaks at 1640 and 792 cm<sup>-1</sup> in these two samples are marked as the C=O stretching vibration and the C–H plane bending vibration [47]. It is worth noting that the peak at 1106 cm<sup>-1</sup> is assigned to C–O stretching vibration and the peak at 617 cm<sup>-1</sup> is related to the Ni–O stretching in the spectrum of PHCSs/NiS-3 sample. These peaks indicate that NiS was chemically bound to the carbon matrix by C–O–Ni bonds [48]. The chemical bonds enhance the strong bond between the carbon matrix and the NiS particles, facilitating the transmission of electrons and ions. Therefore, the electrical conductivity of composite is superior to the corresponding pure carbon material.

The chemical composition and state of the PHCSs/NiS-3 material were measured by XPS analysis (Fig. 5). The broad scan spectrum exhibits the coexistence of the C, Ni and S in Fig. 5a. Two prominent peaks of 854 eV and 872.4 eV of Ni 2*p* are observed in Fig. 5b, indicating two spin–orbit doublets of Ni 2*p*<sub>3/2</sub> and Ni 2*p*<sub>1/2</sub>, accompanied by two related satellite peaks [49]. The energy band difference between these two peaks is about 18.4 eV, strongly confirming the presence of divalent nickel ions. In the spectrum of C 1*s* (Fig. 5c), two center peaks of 284.6 and 286.4 eV represent C=C and C–O, and the peak of 284.9 eV corresponds to C–S, implying that sulfur has entered the crystal lattice of carbon materials [44]. The S 2*p* contains two spin–orbit peaks of 162.9 eV (S 2*p*<sub>3/2</sub>) and 164.1 eV (S 2*p*<sub>1/2</sub>) in Fig. 5d, and the additional peak of 169.5 eV is attributed to Ni–S bond [50]. The above XPS results further demonstrate that the existence of C–O and O–S bonds promotes the connection between the carbon shell and the NiS nanoparticles, which will improve the electrochemical performance of the composite as an electrode.

## Electrochemical performance

The structural details of the PHCSs/NiS composites are sketched in Fig. 6a. Synergistic effect of the unique natural spherical microstructure and the redox reaction of NiS nanoparticles results in remarkable electrochemical performance. During the electrochemical test processes, the Faradaic redox reaction occurred is shown in the following formula [51, 52]:

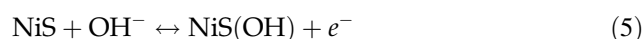
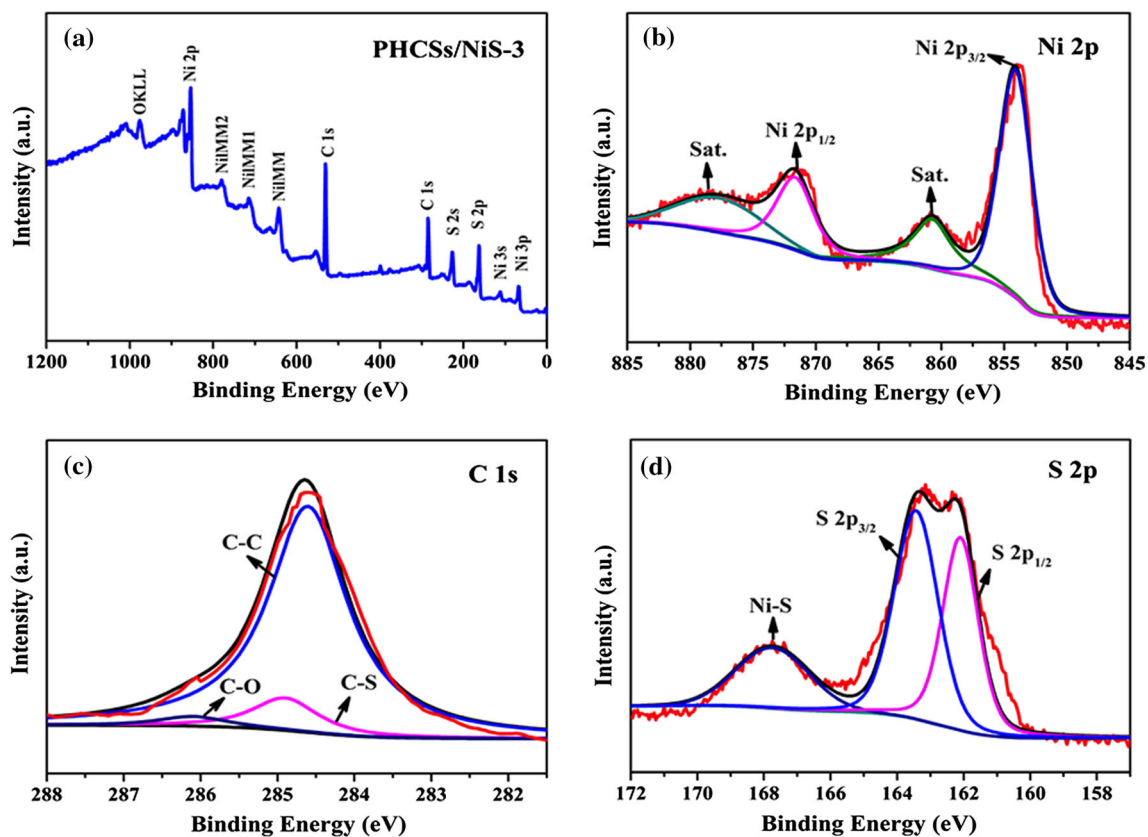
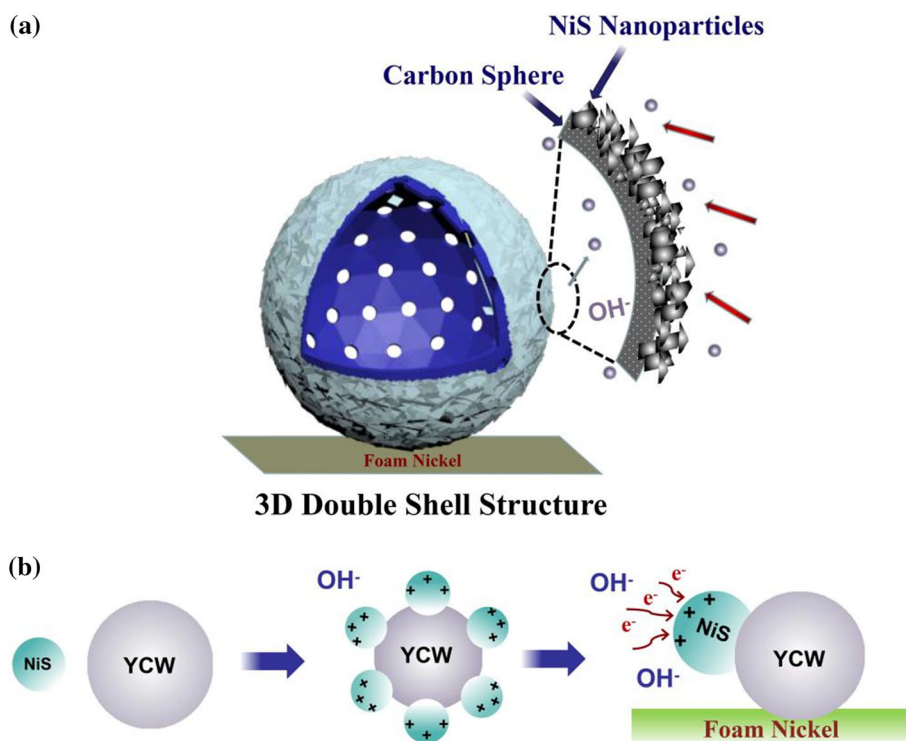


Figure 6b illustrates the electron transportation mechanism of composite materials in the reaction. The OH<sup>-</sup> in the electrolyte solution and NiS in the



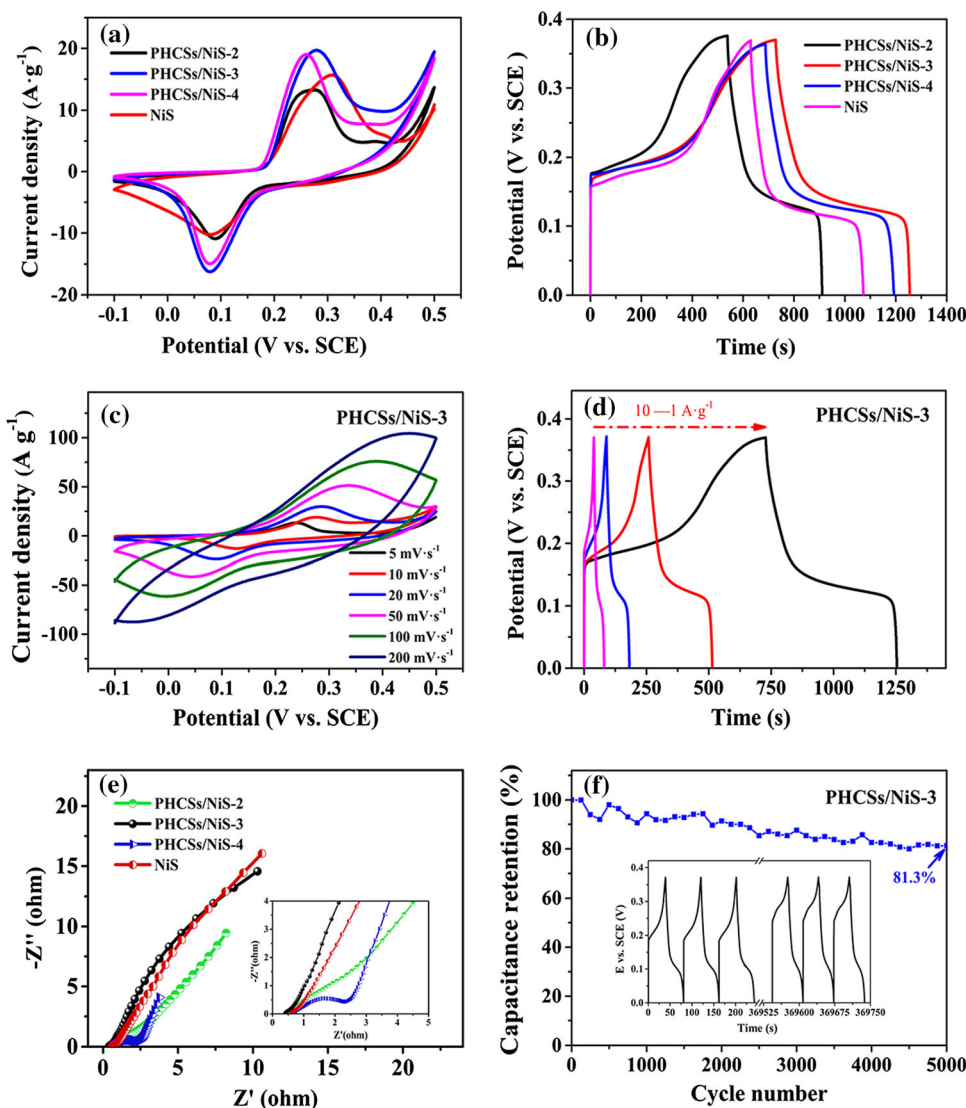
**Figure 5** XPS spectra of the PHCSs/NiS-3. **a** survey spectra, **b** Ni 2p, **c** C 1 s and **(d)** S 2p.

**Figure 6 a** Structural illustration of PHCSs/NiS composite, **b** The electron transportation mechanism of the PHCSs/NiS composite electrodes.





**Figure 7** Electrochemical performances of samples in 6 M KOH electrolyte. **a** CV curves at the scan rate of  $5 \text{ mV s}^{-1}$ , **b** GCD curves at the current density of  $1 \text{ A g}^{-1}$ , **c** CV curves at the different scan rates, **d** GCD curves at the different current densities of PHCSs/NiS-3 sample, **e** Nyquist plots of different samples. **f** Cycle life of PHCSs/NiS-3 sample at the current density of  $10 \text{ A g}^{-1}$ .



electrode material exchange ions, generating an interfacial electric field on the surface of the PHCSs/NiS composites to promote electron transfer during charging/discharging processes [53].

The CV curves of pure NiS nanoparticles and PHCSs/NiS composites at  $5 \text{ mV s}^{-1}$  are shown in Fig. 7a. All samples exhibit distinct redox peaks, which is attributed to the faraday behavior related to redox reactions. The samples have different CV integral areas at the same scanning rate which are clearly observed, indicating that the thickness of NiS deposition influences the electrochemical properties of composites. The PHCSs/NiS-3 has the highest specific capacity, in virtue of the largest integral area. The GCD curves of different samples at  $1 \text{ A g}^{-1}$  are represented in Fig. 7b. The specific capacity values of

PHCSs/NiS-2, PHCSs/NiS-3, PHCSs/NiS-4 and pure NiS are calculated using Eqs. (2) and (3) as  $366.7 \text{ C g}^{-1}$  ( $101.9 \text{ mAh g}^{-1}$ ),  $531.5 \text{ C g}^{-1}$  ( $147.6 \text{ mAh g}^{-1}$ ),  $504.0 \text{ C g}^{-1}$  ( $140.0 \text{ mAh g}^{-1}$ ) and  $445.2 \text{ C g}^{-1}$  ( $123.7 \text{ mAh g}^{-1}$ ), respectively. The specific capacity of PHCSs/NiS-3 composites is the largest because the optimal deposition thickness of NiS provides a greater contribution of capacity. The deposition thickness of NiS in PHCSs/NiS-2 sample is too thin to achieve the ideal performance. For PHCSs/NiS-4 samples, excessive deposition of NiS nanoparticles hinders the transport of ions, resulting in decreased conductivity. Moreover, the specific capacity value of PHCSs/NiS-3 exceeds the pure NiS nanoparticles, which indicates that the carbon spheres effectively prevent the huge volume expansion, inhibit

polymerization of the particles and further accelerate the redox reaction and improve the charge storage ability [54].

Figure 7c presents the CV curves of PHCSs/NiS-3 at 5–200  $\text{mV s}^{-1}$ . The symmetrical redox peaks with similar shapes can be observed, exhibiting the ideal rate capability. When the scan rate reaches 200  $\text{mV s}^{-1}$ , polarization occurs because internal resistance prevents charge collection and ion diffusion [55]. Figure 7d displays the GCD curves of PHCSs/NiS-3 at 0.5–10  $\text{A g}^{-1}$ . Almost symmetrical curves indicate fast and excellent electrochemical reversibility. The specific capacity values of PHCSs/NiS-3 sample are 531.5  $\text{C g}^{-1}$  (147.6  $\text{mAh g}^{-1}$ ), 511.2  $\text{C g}^{-1}$  (142.0  $\text{mAh g}^{-1}$ ), 460.9  $\text{C g}^{-1}$  (128.0  $\text{mAh g}^{-1}$ ) and 412.1  $\text{C g}^{-1}$  (114.5  $\text{mAh g}^{-1}$ ) at 1, 2, 5 and 10  $\text{A g}^{-1}$ , which show excellent rate capability of the material. The Nyquist plots of different materials are revealed in Fig. 7e. The illustration displays the equivalent circuit diagram, which consists of equivalent series resistance ( $R_s$ ), electric double-layer capacitor (Cd), charge transfer resistance ( $R_{ct}$ ) and Warburg impedance ( $Z_w$ ). In the high-frequency region (inset of Fig. 7e), the intercept of the curve and the diameters of semicircles react to the  $R_s$  and  $R_{ct}$  [56–58]. The  $R_s$  values of PHCSs/NiS-2, PHCSs/NiS-3, PHCSs/NiS-4 and NiS are 0.47, 0.39, 0.67 and 0.59  $\Omega$ , respectively. The  $R_{ct}$  values are 3.70, 1.12, 4.02 and 1.28  $\Omega$ , respectively. This indicates that PHCSs/NiS-3 sample has the fastest electron transport speed and the lowest interface charge transfer impedance. In the low-frequency region, the slope reflects the ion diffusion resistance from the electrolyte solution to the electrode interface [59, 60]. The PHCSs/NiS-3 has the least ionic diffusion resistance because of the highest inclination. These results illustrate that PHCSs/NiS-3 has faster ion transport capability and lower resistance.

The long-term GCD test is commonly used to characterize the electrochemical stability of the sample. Figure 7f shows the cycling stability of PHCSs/NiS-3 sample at 10  $\text{A g}^{-1}$ . The PHCSs/NiS-3 composite manifests good cycling stability by maintaining an 81.3% of initial capacitance after 5000 cycles. Initial specific capacitance is decreased rapidly because of the potential shedding of some unbound NiS particles from the carbon matrix. The capacitance almost keeps constant during the 2000–4500th cycle, because the electrode material is more wetted and the electrolyte ions diffuse better into the electrode

resulting in a more complete ion intercalation/deintercalation process [61]. After this stage, a slight continuous increase in specific capacitance can be observed. This interesting phenomenon can be attributed to the further activation of electrode materials during the long-term cycle owing to the increased surface area accessible for electrolyte ions [26, 62].

The SEM and XRD characterizations were performed on the PHCSs/NiS-3 electrode after 5000 cycles. The SEM image (Fig. 8a) shows that the morphology of PHCSs/NiS-3 was almost maintained after a long period of circulation, and no discernible aggregation is found, indicating the superior stability of spherical structure. In Fig. 8b, the XRD pattern confirms the retention of the phase of PHCSs/NiS-3 electrode material after cycling process. The peaks marked with symbols  $\blacklozenge$  and  $\clubsuit$  correspond to the amorphous carbon and Ni foam in the electrode preparation process. After a long-term stability test in 6 M KOH electrolyte, the peak of the composite material was indexed to the initial NiS phase (JCPDS 02-1280) and no other heterogeneous phase was observed, which demonstrates that the phase structure of NiS has not changed during cycling. The above results reveal that PHCSs/NiS-3 composite is a promising electrode material with excellent electrochemical performance. For comparison with the previously reported related electrodes, we calculated the specific capacitance according to Eq. (4). The specific capacitances of PHCSs/NiS-3 designed are 1436.5, 1381.6, 1245.8, and 1113.8  $\text{F g}^{-1}$  at current densities of 1, 2, 5 and 10  $\text{A g}^{-1}$ , respectively. The PHCSs/NiS-3 electrode obtained in this work has comparable or even better electrochemical performance, such as box-in-box hollow structure of  $\beta$ -NiS (668  $\text{F g}^{-1}$  at 1  $\text{A g}^{-1}$ ) [45], nanosheet frame of  $\text{Ni}_3\text{S}_4$  (1213  $\text{F g}^{-1}$  at 2  $\text{A g}^{-1}$ ) [63],  $\text{Ni}_3\text{S}_4$ - $\text{MoS}_2$  heterojunction (985.2  $\text{F g}^{-1}$  at 1  $\text{A g}^{-1}$ ) [64] and  $\text{NiCo}_2\text{S}_4$ -rGO composite (1107  $\text{F g}^{-1}$  at 1  $\text{A g}^{-1}$ ) [65] (for more examples, refer to Table 1).

The hybrid device (PHCSs/NiS-3//AC) was assembled using the PHCSs/NiS-3 as the cathode, the commercial AC as the anode (Fig. 9a). Commercial AC with ideal electrical double-layer behavior has typical operating potential windows of  $-1$  to  $0$  V, and PHCSs/NiS-3 composite has good redox behavior of  $0$  and  $0.5$  V (Fig. 9b). To maintain charge balance, the cathode/anode mass ratio is approximately 1:4.09. CV tests were performed at different

**Figure 8** **a** SEM image of PHCSs/NiS-3 after life cycling test, **b** XRD pattern of PHCSs/NiS-3 after 5000 cycling process.

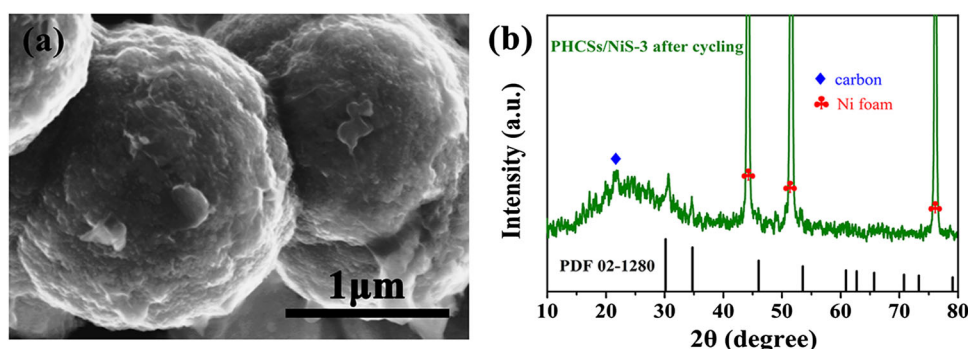


**Table 1** Electrochemical performance of various nickel sulfide-based electrodes in recent typical works under the three-electrode system

Electrode materials	Specific capacitance	Cyclic stability		References
		Retention (%)	Cycles	
NiS microflowers	1127.1 F g <sup>-1</sup> , 1 A g <sup>-1</sup>	97.8	1000	[25]
β-NiS box-in-box hollow structures	668 F g <sup>-1</sup> , 1 A g <sup>-1</sup>	93.4	3000	[52]
Ni <sub>3</sub> S <sub>4</sub> /nanosheet frames	1213 F g <sup>-1</sup> , 2 A g <sup>-1</sup>	60	2000	[63]
Ni <sub>3</sub> S <sub>4</sub> -MoS <sub>2</sub> electrodes	985.21 F g <sup>-1</sup> , 1 A g <sup>-1</sup>	58.2	20,000	[64]
NiCo <sub>2</sub> S <sub>4</sub> -rGO	1107 F g <sup>-1</sup> , 1 A g <sup>-1</sup>	90	5000	[65]
Porous square rod-like NiS <sub>2</sub>	1020.2 F g <sup>-1</sup> , 1 A g <sup>-1</sup>	93.4	1000	[66]
Ni <sub>3</sub> S <sub>2</sub> /CNTs composites	800 F g <sup>-1</sup> , 1 A g <sup>-1</sup>	74.6	1000	[67]
Al-doped β-NiS nanoflowers	1394.6 F g <sup>-1</sup> , 1 A g <sup>-1</sup>	80	2500	[68]
NiCo <sub>2</sub> S <sub>4</sub> hollow nanoprisms	674.8 F g <sup>-1</sup> , 10 A g <sup>-1</sup>	86.5	1500	[69]
3D Ni <sub>3</sub> S <sub>2</sub> /Ni foam	1370.4F g <sup>-1</sup> , 2 A g <sup>-1</sup>	91.4	1000	[70]
Ni <sub>3</sub> S <sub>2</sub> /carbon nanosheets	883 F g <sup>-1</sup> , 2 A g <sup>-1</sup>	83.5	1000	[71]
Porous hollow carbon sphere/NiS composites	1436.9 F g <sup>-1</sup> , 1 A g <sup>-1</sup>	83.3	5000	This work

potential windows to estimate the optimal operating voltage range in Fig. 9c. The CV curves remain stable within 1.5 V; while the voltage window reaches 1.6 V, the electrolyte decomposes significantly and is accompanied by hydrogen/oxygen evolution reactions, which means 1.5 V is an appropriate window. Figure 9d shows the CV curves at different scan rates, with no significant polarization occurring even at 200 mV s<sup>-1</sup>, indicating the remarkable rate capability. The ideally highly linear appearance of the nearly symmetric GCD curve in Fig. 9e demonstrates the electrode has excellent redox reversibility. And the unapparent I-R drop at high current represents the characteristics of low resistance [72]. Figure 9f summarizes the C<sub>s</sub> values of hybrid device at different current densities, which are 78.2, 65.3, 58.8, 58.7, 53.0, and 42.7 F g<sup>-1</sup> at 1, 2, 4, 5, 8 and 10 A g<sup>-1</sup>, implying the good rate capability. Here, the performance of hybrid device is limited by the commercial AC anode material (about 130 F g<sup>-1</sup>).

Therefore, higher capacitance anode materials can further promote the electrochemical performance of device [73].

Energy density (*E*) and power density (*P*) are two critical parameters to characterize the electrochemical properties of supercapacitor device, which can be determined according to Eqs. (3) and (4). Figure 9g exhibits the Ragone plot of PHCSs/NiS-3//AC device. The energy density for hybrid device reaches the maximum of 24.4 Wh kg<sup>-1</sup> at a power density of 767 W kg<sup>-1</sup> and still maintains 13.3 Wh kg<sup>-1</sup> with the power density up to 8263 W kg<sup>-1</sup>. More significantly, the weight energy density is superior to other previously reported sulfide-based hybrid devices, including Ni<sub>3</sub>S<sub>2</sub>/MWCNT-NC//AC (19.8 Wh kg<sup>-1</sup> at 798 W kg<sup>-1</sup>) [67], NiCo<sub>2</sub>S<sub>4</sub>/CFP//AC (17.3 Wh kg<sup>-1</sup> at 180 W kg<sup>-1</sup>) [74], MoS<sub>2</sub>/Ni<sub>3</sub>S<sub>2</sub>//rGO (21.7 Wh kg<sup>-1</sup> at 400 W kg<sup>-1</sup>) [75], NiCoS@N-pCNFs//AC@N-pCNFs (21.6 Wh kg<sup>-1</sup> at 134.9 W kg<sup>-1</sup>) [76]. EIS measurements were performed on PHCSs/NiS-

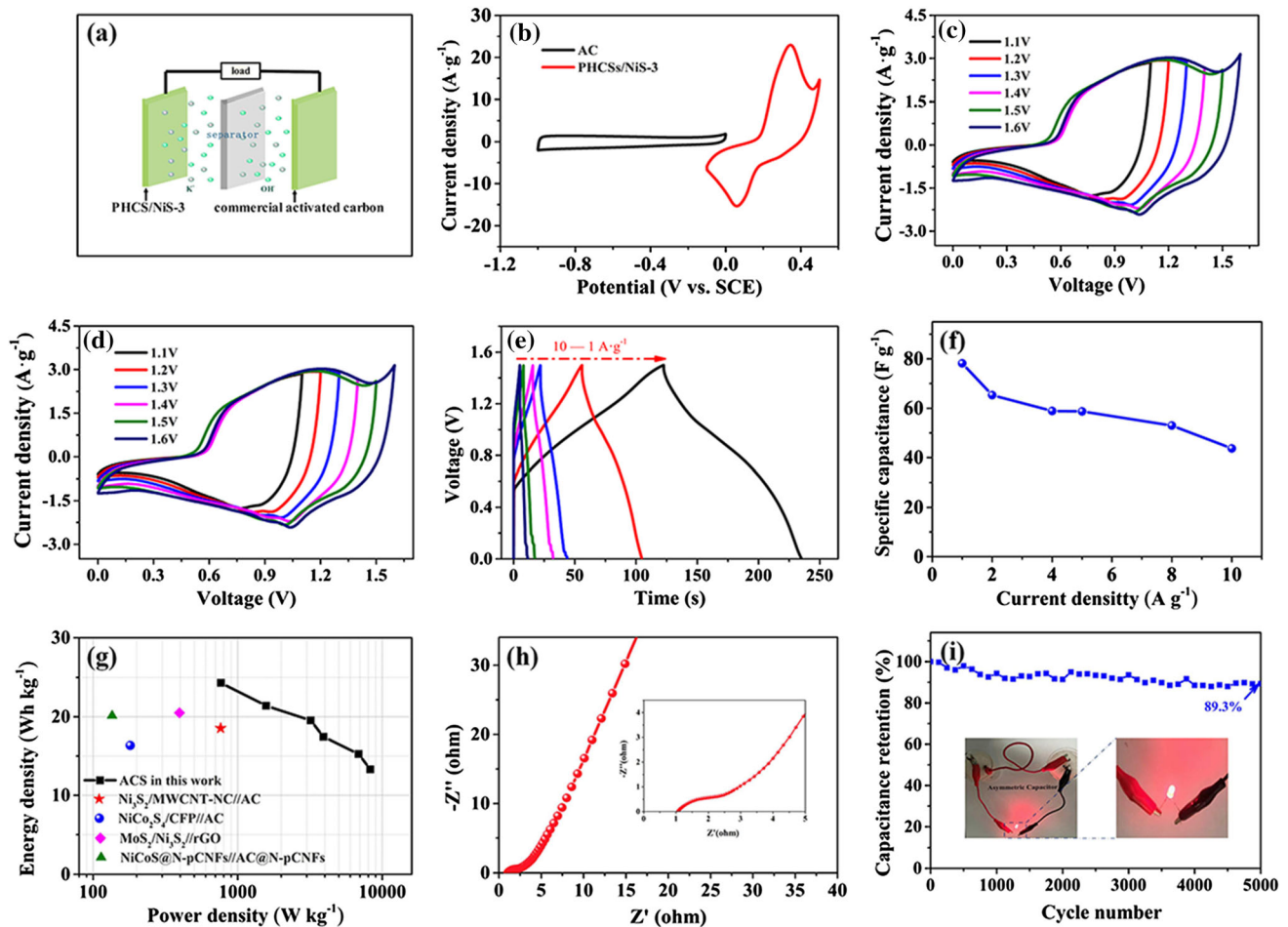


**Figure 9** Electrochemical characterization of PHCSs/NiS-3//AC device. **a** Schematic illustration of the hybrid device configuration, **b** Comparative CV curves of PHCSs and PHCSs/NiS-3 at the scan rate of  $10 \text{ mV s}^{-1}$  in three-electrode system, **c** CV curves in different operation windows at the scan rate of  $20 \text{ mV s}^{-1}$ , **d** CV

curves at the different scan rates. **e** GCD curves at different current densities. **f** The specific capacitance at various current densities, **g** Ragone plot of the hybrid device, **h** Nyquist plot of the hybrid device, **i** cycle stability curve at the current density of  $10 \text{ A g}^{-1}$ .

$3//\text{AC}$  device (Fig. 9h). In the low frequency, larger inclination rate indicates high ion diffusion efficiency. In the amplified high-frequency region, the  $R_s$  of  $1.06 \Omega$  and  $R_{ct}$  of  $2.2 \Omega$  were obtained, which means the high ion diffusion efficiency and favorable charge-transfer power in this system [77]. Figure 9i presents the cycle test result undergoing 5000 continuous GCDs at  $10 \text{ A g}^{-1}$ . An 89.3% capacitor retention rate is still kept after the ultralong 5000 cycles, suggesting outstanding cycle stability of the device. From the internal illustration of Fig. 8i, two charged hybrid devices illuminate a red light-emitting diode (LED), which proves that PHCSs/NiS-3//AC has great potential in practical applications.

## Conclusions

In summary, the litchi shell-like PHCSs/NiS composites were successfully synthesized by facile pyrolysis carbonization and hydrothermal process. Benefiting from the remarkable architecture of PHCSs derived from yeast cell walls and redox performance of NiS, the prepared battery-type electrode possesses the remarkable electrochemical performance. The specific capacitance reaches  $531.5$  and  $412.1 \text{ C g}^{-1}$  at the current densities of  $1$  and  $10 \text{ A g}^{-1}$ , respectively. Furthermore, the assembled PHCSs/NiS-3//AC device delivers a maximum energy density of  $24.4 \text{ Wh kg}^{-1}$  at  $767 \text{ W kg}^{-1}$  and a maximum power density of  $13.3 \text{ Wh kg}^{-1}$  at  $8263 \text{ W kg}^{-1}$ . The capacitance retention of hybrid reaches nearly

89.3% after 5000 cycles. Combining low-cost production with outstanding energy storage performance through a green, simple self-template approach, this material is an attractive candidate for energy storage devices.

## Acknowledgements

This work was supported by research program of the Key Laboratory for Biomedical Effects of Nanomaterials and Nanosafety, Chinese Academy of Sciences (NSKF201908).

## References

- [1] Chu S, Cui Y, Liu N (2016) The path towards sustainable energy. *Nat Mater* 16:16–22. <https://doi.org/10.1038/nmat4834>
- [2] Yang ZF, Tian JR, Yin ZF, Cui CJ, Qian WZ, Wei F (2018) Carbon nanotube- and graphene-based nanomaterials and applications in high-voltage supercapacitor: a review. *Carbon* 141:467–480. <https://doi.org/10.1016/j.carbon.2018.10.010>
- [3] Chen L, Guan LX, Tao JG (2019) Morphology control of Ni<sub>3</sub>S<sub>2</sub> multiple structures and their effect on supercapacitor performances. *J Mater Sci* 54:12737–12746. <https://doi.org/10.1007/s10853-019-03808-x>
- [4] Xie XB, Ni C, Wang BL, Zhang YP, Zhao XJ, Liu L, Wang B, Du W (2019) Recent advances in hydrogen generation process via hydrolysis of Mg-based materials: a short review. *J Alloys Compd* 816:152634. <https://doi.org/10.1016/j.jallcom.2019.152634>
- [5] Chu S, Majumdar A (2012) Opportunities and challenges for a sustainable energy future. *Nature* 488:294–303. <https://doi.org/10.1038/nature11475>
- [6] Mehare MD, Deshmukh AD, Dhoble SJ (2019) Preparation of porous agro-waste-derived carbon from onion peel for supercapacitor application. *J Mater Sci* 55:4213–4224. <https://doi.org/10.1007/s10853-019-04236-7>
- [7] He YM, Chen WJ, Gao CT, Zhou JY, Li XD, Xie EQ (2013) An overview of carbon materials for flexible electrochemical capacitors. *Nanoscale* 5:8799. <https://doi.org/10.1039/c3nr02157b>
- [8] Wu D, Xie XB, Zhang YP, Zhang DM, Du W, Zhang XY, Wang B (2020) MnO<sub>2</sub>/Carbon Composites for Supercapacitor: synthesis and Electrochemical Performance. *Front Mater* 7:2. <https://doi.org/10.3389/fmats.2020.00002>
- [9] Zhao BT, Zhang L, Zhen DX, Yoo S, Ding Y, Chen DC, Chen Y, Zhang QB, Doyle B, Xiong XH, Liu ML (2017) A tailored double perovskite nanofiber catalyst enables ultrafast oxygen evolution. *Nat Commun* 8:14586. <https://doi.org/10.1038/ncomms14586>
- [10] Zhao BT, Zheng Y, Ye F, Deng X, Xu X, Liu M, Shao Z (2015) Multifunctional iron oxide nanoflake/graphene composites derived from mechanochemical synthesis for enhanced lithium storage and electrocatalysis. *ACS Appl Mater Interfaces* 7:14446–14455. <https://doi.org/10.1021/acami.5b03477>
- [11] Li YM, Han X, Yi TF, He YB, Li XF (2019) Review and prospect of NiCo<sub>2</sub>O<sub>4</sub>-based composite materials for supercapacitor electrodes. *J Energy Chem* 31:54–78. <https://doi.org/10.1016/j.jechem.2018.05.010>
- [12] Du W, Wang XN, Zhan J, Sun XQ, Kang LT, Jiang FY, Zhang XY, Shao Q, Dong MY, Liu H, Murugadoss V, Guo ZH (2018) Biological cell template synthesis of nitrogen-doped porous hollow carbon spheres/MnO<sub>2</sub> composites for high-performance asymmetric supercapacitors. *Electrochim Acta* 296:907–915. <https://doi.org/10.1016/j.electacta.2018.11.074>
- [13] Sun Y, Xue JJ, Dong SY, Zhang YD, An YF, Ding B, Zhang TF, Dou H, Zhang XG (2020) Biomass-derived porous carbon electrodes for high-performance supercapacitors. *J Mater Sci* 55:5166–5176. <https://doi.org/10.1007/s10853-019-04343-5>
- [14] Zhang Y, Sun WP, Rui XH, Li B, Tan HT, Guo G, Madhavi S, Zong Y, Yan QY (2015) One-pot synthesis of tunable crystalline Ni<sub>3</sub>S<sub>4</sub>@Amorphous MoS<sub>2</sub> core/shell nanospheres for high-performance supercapacitors. *Small* 11:3694–3702. <https://doi.org/10.1002/smll.201403772>
- [15] Wang HF, Zhang KF, Song YQ, Qiu J, Wu J, Yan LF (2019) MnCo<sub>2</sub>S<sub>4</sub> nanoparticles anchored to N- and S-codoped 3D graphene as a prominent electrode for asymmetric supercapacitors. *Carbon* 146:420–429. <https://doi.org/10.1016/j.carbon.2019.02.035>
- [16] Miniach E, Śliwak A, Moysowicz A, Fernández-García L, González Z, Granda M, Menendez R, Gryglewicz G (2017) MnO<sub>2</sub>/thermally reduced graphene oxide composites for high-voltage asymmetric supercapacitors. *Electrochim Acta* 24:53–62. <https://doi.org/10.1016/j.electacta.2017.04.056>
- [17] Zhao BT, Chen DC, Xiong XH, Song B, Hu RZ, Zhang QB, Rainwater BH, Waller GH, Zhen DX, Ding Y, Chen Y, Qu C, Dang D, Wong CP, Liu ML (2017) A high-energy, long cycle-life hybrid supercapacitor based on graphene composite electrodes. *Energy Storage Mater* 7:32–39. <https://doi.org/10.1016/j.ensm.2016.11.010>
- [18] Zhao BT, Zhang L, Zhang QB, Chen DC, Cheng Y, Deng X, Chen Y, Murphy R, Xiong XH, Song B, Wong CP, Wang MS, Liu ML (2017) Rational design of nickel hydroxide-based nanocrystals on graphene for ultrafast energy storage.

- Adv Energy Mater 8:1702247. <https://doi.org/10.1002/aenm.201702247>
- [19] Dai SG, Zhao BT, Qu C, Chen DC, Dang D, Song B, deGlee BM, Fu JW, Hu CG, Wong CP, Liu ML (2017) Controlled synthesis of three-phase Ni<sub>x</sub>S<sub>y</sub>/rGO nanoflake electrodes for hybrid supercapacitors with high energy and power density. *Nano Energy* 33:522–531. <https://doi.org/10.1016/j.nanoen.2017.01.056>
- [20] Guo W, Wang JY, Fan C, Chen Z, Liu P, Zhu DJ, Xu ZL, Pang L, Li T (2017) Synthesis of carbon self-repairing porous g-C<sub>3</sub>N<sub>4</sub> nanosheets/NiCo<sub>2</sub>S<sub>4</sub> nanoparticles hybrid composite as high-performance electrode materials for supercapacitors. *Electrochim Acta* 253:68–77. <https://doi.org/10.1016/j.electacta.2017.09.025>
- [21] Meng XY, Cao Q, Jin L, Zhang XH, Gong SL, Li P (2017) Carbon electrode materials for supercapacitors obtained by co-carbonization of coal-tar pitch and sawdust. *J Mater Sci* 52:760–769. <https://doi.org/10.1007/s10853-016-0370-1>
- [22] Chen FS, Wang H, Ji S, Linkov V, Wang RF (2019) High-performance all-solid-state asymmetric supercapacitors based on sponge-like NiS/Ni<sub>3</sub>S<sub>2</sub> hybrid nanosheets. *Mater Today Energy* 11:211–217. <https://doi.org/10.1016/j.mtener.2018.12.002>
- [23] Zhang D, Sun WP, Zhang Y, Dou YH, Jiang YZ, Dou SX (2016) Engineering hierarchical hollow nickel sulfide spheres for high-performance sodium storage. *Adv Funct Mater* 26:7479–7485. <https://doi.org/10.1002/adfm.201602933>
- [24] Wang K, Yan R, Tian XD, Wang Y, Lei SW, Li X, Yang T, Wang XJ, Song Y, Liu YQ, Liu ZJ, Guo QG (2019) Multi-scale biomass-based carbon microtubes decorated with Ni-Co sulphides nanoparticles for supercapacitors with high rate performance. *Electrochim Acta* 302:78–91. <https://doi.org/10.1016/j.electacta.2019.02.015>
- [25] Yang JQ, Duan XC, Guo W, Li D, Zhang HL, Zheng WJ (2014) Electrochemical performances investigation of NiS/rGO composite as electrode material for supercapacitors. *Nano Energy* 5:74–81. <https://doi.org/10.1016/j.nanoen.2014.02.006>
- [26] Peng L, Ji X, Wan HZ, Ruan YJ, Xu K, Chen C, Miao L, Jiang JJ (2015) Nickel Sulfide nanoparticles synthesized by microwave-assisted method as promising supercapacitor electrodes: an experimental and computational study. *Electrochim Acta* 182:361–367. <https://doi.org/10.1016/j.electacta.2015.09.024>
- [27] Yan XY, Tong XL, Ma L, Tian YM, Cai YS, Gong CW, Zhang MG, Liang LP (2014) Synthesis of porous NiS nanoflake arrays by ion exchange reaction from NiO and their high performance supercapacitor properties. *Mater Lett* 124:133–136. <https://doi.org/10.1016/j.matlet.2014.03.067>
- [28] Yang JQ, Guo W, Li D, Wei CY, Fan HM, Wu LY, Zheng WJ (2014) Synthesis and electrochemical performances of novel hierarchical flower-like nickel sulfide with tunable number of composed nanoplates. *J Power Sour* 268:113–120. <https://doi.org/10.1016/j.jpowsour.2014.06.030>
- [29] Ma X, Zhang L, Xu GC, Zhang CY, Song HJ, He YT, Zhang C, Jia DZ (2017) Facile synthesis of NiS hierarchical hollow cubes via Ni formate frameworks for high performance supercapacitors. *Chem Eng J* 320:22–28. <https://doi.org/10.1016/j.cej.2017.03.033>
- [30] Laatikainen M, Sainio T (2019) Ion exchange in complexing media—Nickel removal from ammoniacal ammonium sulfate solutions. *Chem Eng J* 373:831–839. <https://doi.org/10.1016/j.cej.2019.05.128>
- [31] Du DW, Lan R, Humphreys J, Amari H, Tao S (2018) Preparation of nanoporous nickel copper sulfide on carbon cloth for high-performance hybrid supercapacitors. *Electrochim Acta* 273:170–180. <https://doi.org/10.1016/j.electacta.2018.04.041>
- [32] Zhang LL, Zhao XS (2009) Carbon-based materials as supercapacitor electrodes. *Chem Soc Rev* 38:2520. <https://doi.org/10.1039/b813846j>
- [33] Deng X, Zhao BT, Zhu L, Shao ZP (2015) Molten salt synthesis of nitrogen-doped carbon with hierarchical pore structures for use as high-performance electrodes in supercapacitors. *Carbon* 93:48–58. <https://doi.org/10.1016/j.carbon.2015.05.031>
- [34] Cai F, Sun R, Kang YR, Chen HY, Chen MH, Li QW (2015) One-step strategy to a three-dimensional NiS-reduced graphene oxide hybrid nanostructure for high performance supercapacitors. *RSC Adv* 5:23073–23079. <https://doi.org/10.1039/c5ra02058a>
- [35] Sun CC, Ma MZ, Yang J, Zhang YF, Chen P, Huang W, Dong XC (2014) Phase-controlled synthesis of  $\alpha$ -NiS nanoparticles confined in carbon nanorods for high performance supercapacitors. *Sci Rep* 4:7054. <https://doi.org/10.1038/srep07054>
- [36] Reddy BJ, Vickraman P, Justin AS (2019) Electrochemical performance of nitrogen-doped graphene anchored nickel sulfide nanoflakes for supercapacitors. *Appl Surf Sci* 483:1142–1148. <https://doi.org/10.1016/j.apsusc.2019.03.292>
- [37] Wang S, Sun W, Yang DS, Yang F (2019) Conversion of soybean waste to sub-micron porous-hollow carbon spheres for supercapacitor via a reagent and template-free route. *Mater Today Energy* 13:50–55. <https://doi.org/10.1016/j.mtener.2019.04.015>
- [38] Sauer M, Porro D, Mattanovich D, Branduardi P (2010) 16 years research on lactic acid production with yeast—ready for

- the market? *Biotechnol Genet Eng Rev* 27:229–256. <https://doi.org/10.1080/02648725.2010.10648152>
- [39] Yang QJ, Liu Y, Yan M, Lei Y, Shi WD (2019) MOF-derived hierarchical nanosheet arrays constructed by interconnected NiCo-alloy@NiCo-sulfide core-shell nanoparticles for high-performance asymmetric supercapacitors. *Chem Eng J* 370:666–676. <https://doi.org/10.1016/j.cej.2019.03.239>
- [40] Liu X, Li Q, Zhao Y, Dong Y, Fan Q, Kuang Q (2017) A promising mechanical ball-milling method to synthesize carbon-coated  $\text{Co}_9\text{S}_8$  nanoparticles as high-performance electrode for supercapacitor. *J Mater Sci* 52:13552–13560. <https://doi.org/10.1007/s10853-017-1373-2>
- [41] Wang LC, Gao L, Wang J, Shen Y (2019)  $\text{MoO}_3$  nanobelts for high-performance asymmetric supercapacitor. *J Mater Sci* 54:13685–13693. <https://doi.org/10.1007/s10853-019-03836-7>
- [42] Xie YP, Fang L, Cheng HW, Hu CJ, Zhao HB, Xu JQ, Fang JH, Lu XG, Zhang JJ (2016) Biological cell derived N-doped hollow porous carbon microspheres for lithium–sulfur batteries. *J Mater Chem A* 4:15612–15620. <https://doi.org/10.1039/c6ta06164h>
- [43] Justin AS, Vickraman P, Reddy BJ (2019) Carbon Sphere@Nickel sulfide core-shell nanocomposite for high performance supercapacitor application. *Curr Appl Phys* 19:295–302. <https://doi.org/10.1016/j.cap.2018.12.010>
- [44] Wang DW, Xu Wang YT, Xu W (2018) Rational synthesis of porous carbon nanocages and their potential application in high rate supercapacitors. *J Electroanal Chem* 815:166–174. <https://doi.org/10.1016/j.jelechem.2018.03.016>
- [45] Zhang Y, Liu SS, Zheng XY, Wang X, Xu Y, Tang HQ, Kang FY, Yang QH, Luo JY (2017) Biomass organs control the porosity of their pyrolyzed carbon. *Adv Funct Mater* 27:1604687. <https://doi.org/10.1002/adfm.201604687>
- [46] Zhang JC, Xu CY, Zhang DJ, Zhao JL, Zheng SX, Su HM, Wei FF, Yuan BQ, Fernandez C (2017) Facile synthesis of a nickel sulfide (NiS) hierarchical flower for the electrochemical oxidation of  $\text{H}_2\text{O}_2$  and the methanol oxidation reaction (MOR). *J Electrochem Soc* 164:B92–B96. <https://doi.org/10.1149/2.0221704jes>
- [47] Dirican M, Yanilmaz M, Zhang X (2014) Free-standing polyaniline–porous carbon nanofiber electrodes for symmetric and asymmetric supercapacitors. *RSC Adv* 4:59427–59435. <https://doi.org/10.1039/c4ra09103e>
- [48] Li Y, An FF, Wu HR, Zhu SM, Lin CYZ, Xia MD, Xu K, Zhang D, Lian K (2019) A  $\text{NiCo}_2\text{S}_4$ /hierarchical porous carbon for high performance asymmetrical supercapacitor. *J Power Sour* 427:138–144. <https://doi.org/10.1016/j.jpowsour.2019.04.060>
- [49] Tran VC, Sahoo S, Shim JJ (2018) Room-temperature synthesis of NiS hollow spheres on nickel foam for high-performance supercapacitor electrodes. *Mater Lett* 210:105–108. <https://doi.org/10.1016/j.matlet.2017.08.136>
- [50] Gu HH, Huang YP, Zuo LZ, Fan W, Liu TX (2016) Electrospun carbon nanofiber@ $\text{CoS}_2$  core/sheath hybrid as an efficient all-pH hydrogen evolution electrocatalyst. *Inorg Chem Front* 3:1280–1288. <https://doi.org/10.1039/c6qi00229c>
- [51] Guan B, Li Y, Yin BY, Liu KF, Wang DW, Zhang HH, Cheng CJ (2017) Synthesis of hierarchical NiS microflowers for high performance asymmetric supercapacitor. *Chem Eng J* 308:1165–1173. <https://doi.org/10.1016/j.cej.2016.10.016>
- [52] Yu XY, Yu L, Shen LF, Song XH, Chen HY, Lou XW (2015) General formation of MS (M = Ni, Cu, Mn) box-in-box hollow structures with enhanced pseudocapacitive properties. *Adv Funct Mater* 24:7440–7446. <https://doi.org/10.1002/adfm.201402560>
- [53] Zhao X, Sui JH, Li F, Fang HT, Wang HG, Li JY, Cai W, Cao GZ (2016) Lamellar  $\text{MoSe}_2$  nanosheets embedded with  $\text{MoO}_2$  nanoparticles: novel hybrid nanostructures promoted excellent performances for lithium ion batteries. *Nanoscale* 8:17902–17910. <https://doi.org/10.1039/c6nr05584b>
- [54] Liu YP, Li ZL, Yao L, Chen SM, Zhang PX, Deng LB (2019) Confined growth of  $\text{NiCo}_2\text{S}_4$  nanosheets on carbon flakes derived from eggplant with enhanced performance for asymmetric supercapacitors. *Chem Eng J* 366:550–559. <https://doi.org/10.1016/j.cej.2019.02.125>
- [55] Li ZP, Mi YJ, Liu XH, Liu S, Yang SR, Wang JQ (2011) Flexible graphene/ $\text{MnO}_2$  composite papers for supercapacitor electrodes. *J Mater Chem* 21:14706–14711. <https://doi.org/10.1039/c1jm11941a>
- [56] Hou CX, Tai ZX, Zhao LL, Zhai YJ, Hou Y, Fan YQ, Dang F, Wang J, Liu HK (2018) High performance  $\text{MnO}@\text{C}$  microcages with a hierarchical structure and tunable carbon shell for efficient and durable lithium storage. *J Mater Chem A* 6:9723–9736. <https://doi.org/10.1039/c8ta02863j>
- [57] Hou CX, Hou Y, Fan YQ, Zhai YJ, Wang Y, Sun ZY, Fan RH, Dang F, Wang J (2018) Oxygen vacancy derived local build-in electric field in mesoporous hollow  $\text{Co}_3\text{O}_4$  microspheres promotes high-performance Li-ion batteries. *J Mater Chem A* 6:6967–6976. <https://doi.org/10.1039/c8ta00975a>
- [58] Hou CX, Wang J, Du W, Wang JC, Du Y, Liu CT, Zhang JX, Hou H, Dang F, Zhao LL, Guo ZH (2019) One-pot synthesized molybdenum dioxide–molybdenum carbide heterostructures coupled with 3D holey carbon nanosheets for highly efficient and ultrastable cycling lithium-ion storage. *J Mater Chem A* 7:13460–13472. <https://doi.org/10.1039/c9ta03551f>
- [59] Du W, Wang XN, Ju XY, Xu K, Gao MJ, Zhang XT (2017) Carbonized *Enteromorpha prolifera* with porous architecture and its polyaniline composites as high-performance

- electrode materials for supercapacitors. *J Electroanal Chem* 802:15–21. <https://doi.org/10.1016/j.jelechem.2017.08.044>
- [60] Gou J (2017) Ni<sub>2</sub>P/NiS<sub>2</sub> composite with phase boundaries as high-performance electrode material for supercapacitor. *J Electrochem Soc* 164:A2956–A2961. <https://doi.org/10.1149/2.0281713jes>
- [61] Sun PX, Li N, Wang CG, Yin JM, Zhao G, Hou PY, Xu XJ (2019) Nickel–cobalt based aqueous flexible solid state supercapacitors with high energy density by controllable surface modification. *J Power Sour* 427:56–61. <https://doi.org/10.1016/j.jpowsour.2019.04.062>
- [62] Cheng LL, Hu YY, Ling L, Qiao DD, Cui SC, Jiao Z (2018) One-step controlled synthesis of hierarchical hollow Ni<sub>3</sub>S<sub>2</sub>/NiS@Ni<sub>3</sub>S<sub>4</sub> core/shell submicrospheres for high-performance supercapacitors. *Electrochim Acta* 283:664–675. <https://doi.org/10.1016/j.electacta.2018.07.013>
- [63] Wang LN, Liu JJ, Zhang LL, Dai BS, Xu M, Ji MW, Zhao XS, Cao CB, Zhang JT, Zhu HS (2015) Rigid three-dimensional Ni<sub>3</sub>S<sub>4</sub> nanosheet frames: controlled synthesis and their enhanced electrochemical performance. *RSC Adv* 5:8422–8426. <https://doi.org/10.1039/c4ra15607b>
- [64] Luo WH, Zhang GF, Cui YX, Sun Y, Qin Q, Zhang J, Zheng WJ (2017) One-step extended strategy for the ionic liquid-assisted synthesis of Ni<sub>3</sub>S<sub>4</sub>–MoS<sub>2</sub> heterojunction electrodes for supercapacitors. *J Mater Chem A* 5:11278–11285. <https://doi.org/10.1039/c7ta02268a>
- [65] Fan YM, Liu YC, Liu XB, Liu YN, Fan LZ (2017) Hierarchical porous NiCo<sub>2</sub>S<sub>4</sub>–rGO composites for high-performance supercapacitors. *Electrochim Acta* 249:1–8. <https://doi.org/10.1016/j.electacta.2017.07.175>
- [66] Ruan YJ, Jiang JJ, Wan HZ, Ji X, Miao L, Peng L, Zhang B, Lv L, Liu J (2016) Rapid self-assembly of porous square rod-like nickel persulfide via a facile solution method for high-performance supercapacitors. *J Power Sour* 301:122–130. <https://doi.org/10.1016/j.jpowsour.2015.09.116>
- [67] Dai CS, Chien PY, Lin JY, Chou SW, Wu WK, Li PH, Wu KY, Lin TW (2013) Hierarchically structured Ni<sub>3</sub>S<sub>2</sub>/carbon nanotube composites as high performance cathode materials for asymmetric supercapacitors. *ACS Appl Mater Interfaces* 5:12168–12174. <https://doi.org/10.1021/am404196s>
- [68] Ruan YJ, Zha D, Lv L, Zhang B, Liu J, Ji X, Wang CD, Jiang JJ (2017) Al-doped β-NiS mesoporous nanoflowers for hybrid-type electrodes toward enhanced electrochemical performance. *Electrochim Acta* 236:307–318. <https://doi.org/10.1016/j.electacta.2017.03.140>
- [69] Yu L, Zhang L, Wu HB, Lou XW (2014) Formation of Ni<sub>x</sub>Co<sub>3-x</sub>S<sub>4</sub> hollow nanoprisms with enhanced pseudocapacitive properties. *Angew Chem Int Ed* 53:3711–3714. <https://doi.org/10.1002/anie.201400226>
- [70] Huo HH, Zhao YQ, Xu CL (2014) 3D Ni<sub>3</sub>S<sub>2</sub> nanosheet arrays supported on Ni foam for high-performance supercapacitor and non-enzymatic glucose detection. *J Mater Chem A* 2:15111. <https://doi.org/10.1039/c4ta02857k>
- [71] Zhu BT, Wang ZY, Ding S, Chen JS, Lou XW (2011) Hierarchical nickel sulfide hollow spheres for high performance supercapacitors. *RSC Adv* 1:397. <https://doi.org/10.1039/c1ra00240f>
- [72] Liu SD, Jun SC (2017) Hierarchical manganese cobalt sulfide core–shell nanostructures for high-performance asymmetric supercapacitors. *J Power Sour* 342:629–637. <https://doi.org/10.1016/j.jpowsour.2016.12.057>
- [73] Wang MQ, Li ZQ, Wang CX, Zhao RZ, Li CX, Guo DX, Zhang LY, Yin LW (2017) Novel core-shell FeOF/Ni(OH)<sub>2</sub> hierarchical nanostructure for all-solid-state flexible supercapacitors with enhanced performance. *Adv Funct Mater* 27:1701014. <https://doi.org/10.1002/adfm.201701014>
- [74] Xiong XH, Waller G, Ding D, Chen DC, Rainwater B, Zhao B, Wang ZX, Liu ML (2015) Controlled synthesis of NiCo<sub>2</sub>S<sub>4</sub> nanostructured arrays on carbon fiber paper for high-performance pseudocapacitors. *Nano Energy* 16:71–80. <https://doi.org/10.1016/j.nanoen.2015.06.018>
- [75] Huang L, Hou HJ, Liu BC, Zeinu K, Zhu XL, Yuan XQ, He XL, Wu LS, Hu JP, Yang JK (2017) Ultrahigh-performance pseudocapacitor based on phase-controlled synthesis of MoS<sub>2</sub> nanosheets decorated Ni<sub>3</sub>S<sub>2</sub> hybrid structure through annealing treatment. *Appl Surf Sci* 425:879–888. <https://doi.org/10.1016/j.apsusc.2017.06.334>
- [76] Liu YK, Lu QL, Huang Z, Sun SQ, Yu B, Evariste U, Jiang GH, Yao JM (2018) Electrodeposition of NiCoS nanosheet arrays on N-doped porous carbon nanofibers for flexible asymmetric supercapacitors. *J Alloys Compd* 762:301–311. <https://doi.org/10.1016/j.jallcom.2018.05.239>
- [77] Zhang K, Wang QG, Thota A, Zhang WZ, Chen J, Wang Y, Wu XM, Wang SM (2020) Flexible 3D hierarchical porous NiCo<sub>2</sub>O<sub>4</sub>/CC electrode decorated by nitrogen-doped carbon from polyaniline carbonization for high-performance supercapacitors. *J Mater Sci* 55:5982–5993. <https://doi.org/10.1007/s10853-020-04403-1>

**Publisher's Note** Springer Nature remains neutral with regard to jurisdictional claims in published maps and institutional affiliations.